Floquet spectrum and electronic transitions of tilted anisotropic Dirac materials under electromagnetic radiation: monodromy matrix approach.

A. Kunold,[1, *] J. C. Sandoval-Santana,[2, †] V. G. Ibarra-Sierra,[3, ‡] and Gerardo G. Naumis[3, §]

[1]*Área de Física Teórica y Materia Condensada, Universidad Autónoma Metropolitana*
Azcapotzalco, Av. San Pablo 180, Col. Reynosa-Tamaulipas, 02200 Cuidad de México, México
[2]*Instituto de Física, Universidad Nacional Autónoma de México, Apartado Postal 20-364, 01000, Ciudad de México, México*
[3]*Departamento de Sistemas Complejos, Instituto de Fisica, Universidad Nacional*
Autónoma de México, Apartado Postal 20-364,01000, Ciudad de México, México.

(Dated: April 28, 2020)

We analyze the quasienergy-spectrum and the valence to conduction-band transition probabilities of a tilted anisotropic Dirac material subject to linearly and circularly polarized electromagnetic fields. The quasienergy-spectrum is numerically calculated from the monodromy matrix of the Schrödinger equation via the Floquet theorem for arbitrarily intense electromagnetic fields. To asses the valence to conduction-band transition times we deduced a Rabi-like formula in the rotating wave approximation. In the strong-field regime the spectrum as a function of the momentum components divides into two very distinctive regions. In the first, located around the Dirac point, the quasi-spectrum is significantly distorted by the field as the electronic parameters are renormalized by electronic-dressing. In the second, all the characteristics of the free carrier spectrum are retained. Linearly polarized light anisotropically deforms the spectrum according to the field polarization direction. Dirac-like points form around the original Dirac point. The quasi-spectrum of circularly polarized light, instead, exhibits a gap formation in the Dirac point and has elliptical symmetry. We show that, in contrast to the single-photon resonant transitions that characterize the weak-field regime, the strong-field regime is dominated by multiphoton resonances.

I. INTRODUCTION

The extraordinary electronic and optical properties of graphene make it an ideal platform for the development of diverse optoelectronic devices and applications[1–3] such as THz generators[4], plasmonic devices[5,6], polarization-sensitive, broad band photodectectors[7,8], broad band optical modulators[9–11], infrared photodetectors[12] and solar cells[13,14].

Because of its broadband and ultrafast optical response and weak screening[15], graphene is a particularly attractive material for the implementation of attosecond science applications[8,16–18]. This field has been rapidly growing[19] since the first demonstration of sub-femtosecond pulse generation[20] with the prospect of new time-resolved spectroscopic techniques and overcoming the speed limitations of electronics[19]. These applications rely on the high light-matter coupling between carriers and strong optical fields.

The limit of strong electromagnetic fields is of great interest also because it may give rise to exotic and novel quantum phases coherently induced by light. Two striking examples of Floquet-engineered topological phases in graphene are the Photovoltaic Hall effect[21] and the light-induced anomalous Hall effect[22]. Astonishingly the Hall effect, produced in the absence of a magnetic field, arises from a light-induced Berry curvature absent in the static case[22]. The dressing of electrons, i.e. electrons bounded to a strong electromagnetic field[1,12,23–31], has become a key concept in understanding the interaction of electromagnetic radiation with charge carriers in graphene[23,28,32]. Electromagnetic dressing substantially renormalizes the energy spectrum as well as other electronic parameters of graphene[28,30,31,33] and could, therefore, be exploited to adjust its optoelectronic properties.

Unlike metals, semiconductors and other conventional materials used in electronics, Dirac materials have a linear dispersion relation near the band edge that can be characterized by the Dirac Hamiltonian. This hinders the application of some of the standard solid-state theoretical tools. Such is the case of carriers interacting with a strong electromagnetic field. The purpose of this paper is to analyze the dynamics of electrons in a Dirac material coupled to an intense electromagnetic field, and at the same time, to introduce a numerical technique to find the temporal evolution of quantum, systems.

The research presented here is a follow up of our previous work concerning electromagnetic waves in the strong field regime acting on borophene[34,35]. The methods and results introduced in this paper are of a far more general character. In former investigations we were only able to tackle the strong-field regime in an approximate manner, due to the lack of a method capable to bridge the gap between the low and high electromagnetic field intensity. In this work we have developed methods that allow us to approach the calculations of the quasienergy-spectrum, time-dependent wave function and transition probabilities without any restrictions in field parameters such as polarization, intensity and time duration. These methods allow us to continuously go from the weak to the strong-field regime without any approximations. This is a fundamental requirement in the comparison of spectra and transition probabilities in both regimes. Moreover, the deviced methods open the door to the study of many other time-driven quantum systems[36–38].

We center our discussion in the effects on the

quasienergy spectrum and the valence to conduction band transition probability. In order for our study to be general enough we utilize the low energy Hamiltonian of an anisotropic tilted Dirac material. Specifically, we present results for borophene[34,39–41], the paradigmatic example of tilted Dirac materials. For the sake of comparison, we calculated the quasi-spectra in the weak and strong-field regimes for linearly and circularly polarized light.

We show that, regardless of the field polarization, under strong illumination the quasi-spectrum can be separated in two very well defined regions in $\boldsymbol{k}$-space. The first, where the electromagnetic field is perturbative, resembles that of the free carrier spectrum. In the second, where the field effects are more dramatic, new Dirac-like points as well as gaps are generated. The boundary where the sharp transition from one regime to the other takes place is accurately determined. Under circularly polarized light we clearly demonstrate the emergence of a gap in the Dirac point. In the strong field region, an anisotropic quasi-spectrum emerges for linearly polarized light. The anisotropy is oriented in accordance with the filed polarization direction. We demonstrate that, in stark contrast with the perturbative regime, where transitions happen between energy levels whose energy difference match the photon energy, in the strong field regime they take place well outside the single photon resonance condition. This indicates the presence of multiphoton excitations.

The paper is organized as follows. In Sec. II we introduce the low energy Hamiltonian of a 2D tilted anisotropic Dirac material, while in Sec. III we set up the basic equations for the model system under an electromagnetic field with arbitrary polarization. A method to compute the quasienergy-spectrum via the Floquet theorem and the monodromy matrix is presented in Sec. IV. Section V is devoted to the derivation of a Rabi-like formula by adopting the rotating wave approximation. A comparison between the diverse quasienergy-spectra and valence to conduction-band transition probabilities under different illumination conditions is shown in Sec. VI, while a discussion of the results is presented in Sec. VII. We conclude and summarize in VIII.

II. TILTED ANISOTROPIC DIRAC HAMILTONIAN MODEL

The $\boldsymbol{K}$ valley low energy Hamiltonian of a 2D tilted anisotropic Dirac material is given by[34,35,40,42,43]

$$\mathcal{H}_0 = v_t p_y \sigma_0 + v_x p_x \sigma_x + v_y p_y \sigma_y, \qquad (1)$$

where σ_0 is the 2×2 identity matrix, $\sigma_{x,y}$ are the Pauli matrices, $p_{x,y}$ are the components of the 2D momentum operator $\boldsymbol{p}$ and v_x, v_y are the anisotropic Fermi velocities. The velocity v_t gives the tilting of the energy dispersion with respect to the energy axis[40,42]. The well

known graphene energy dispersion is recovered by setting $v_t = 0$ and $v_x = v_y = v_F \approx c/300 \approx 10^6\, m/s$ with v_F and c being the Fermi velocity[42] and the speed of light respectively. In 8-$Pmmm$ borophene, such velocities are $v_t = 0.32 v_F$, $v_x = 0.86 v_F$ and $v_y = 0.69 v_F$. To simplify the presentation, from here on, we restrict our calculations to the $\boldsymbol{K}$ valley. To retrieve the expressions corresponding to the $\boldsymbol{K}'$ valley it suffices to invert the sing of v_t. The sings of v_x and v_y depend on the chosen basis[40]. The free electron wave function corresponding to (1) is given by the spinor

$$\Psi_\eta(\boldsymbol{r}) = \frac{\exp(i\boldsymbol{k} \cdot \boldsymbol{r})}{\sqrt{2}} \begin{pmatrix} 1 \\ \eta \mathrm{e}^{i\theta(\boldsymbol{k})} \end{pmatrix}, \qquad (2)$$

where k_x and k_y are the wave vector $\boldsymbol{k}$ components, $\theta(\boldsymbol{k}) = \tan^{-1}(v_y k_y / v_x k_x)$ and $\eta = \pm 1$ is the band index. The eigenenergies associated with this wave function are

$$\mathcal{E}_\eta(\boldsymbol{k}) = \hbar v_t k_y + \eta \epsilon(\boldsymbol{k}), \qquad (3)$$

where

$$\epsilon(\boldsymbol{k}) = \hbar \sqrt{v_x^2 k_x^2 + v_y^2 k_y^2}. \qquad (4)$$

It is important here to underline that the Hamiltonian matrix (1), as well as the wave function vector (2), are expanded in terms of the sublattice state basis.

III. TILTED ANISOTROPIC DIRAC MATERIALS UNDER AN ELLIPTICALLY POLARIZED FIELD

Under the action of a normally incident electromagnetic plane wave, the Hamiltonian (1) transforms according to the Peierls substitution $\boldsymbol{p} \to \boldsymbol{p} - e\boldsymbol{A}$ as[44]

$$\mathcal{H} = v_t \left(p_y - e A_y \right) \sigma_0 \\ + v_x \left(p_x - e A_x \right) \sigma_x + v_y \left(p_y - e A_y \right) \sigma_y, \quad (5)$$

where $\boldsymbol{A} = A_x \hat{\boldsymbol{\imath}} + A_y \hat{\boldsymbol{\jmath}}$ is the radiation vector potential. It is convenient to adopt a gauge in which the vector potential only depends on time as

$$\boldsymbol{A}(t) = -\frac{E_x}{\omega} \cos\left(\omega t + \delta\right) \hat{\boldsymbol{\imath}} - \frac{E_y}{\omega} \cos\left(\omega t + \delta + \phi\right) \hat{\boldsymbol{\jmath}}, \quad (6)$$

where ω is the angular frequency of the radiation. For $E_x = E_y$ the parameter ϕ allows to continuously vary the field polarization from linear ($\phi = 0$) to circular ($\phi = \pm\pi/2$). The initial field phase is given by δ. We drop the initial phase δ for the moment and will restore it later by doing $\omega t \to \omega t + \delta$. The electric field of the electromagnetic wave is given by

$$\boldsymbol{E} = -\frac{\partial \boldsymbol{A}}{\partial t} = -E_x \sin\left(\omega t\right) \hat{\boldsymbol{\imath}} - E_y \sin\left(\omega t + \phi\right) \hat{\boldsymbol{\jmath}}. \quad (7)$$
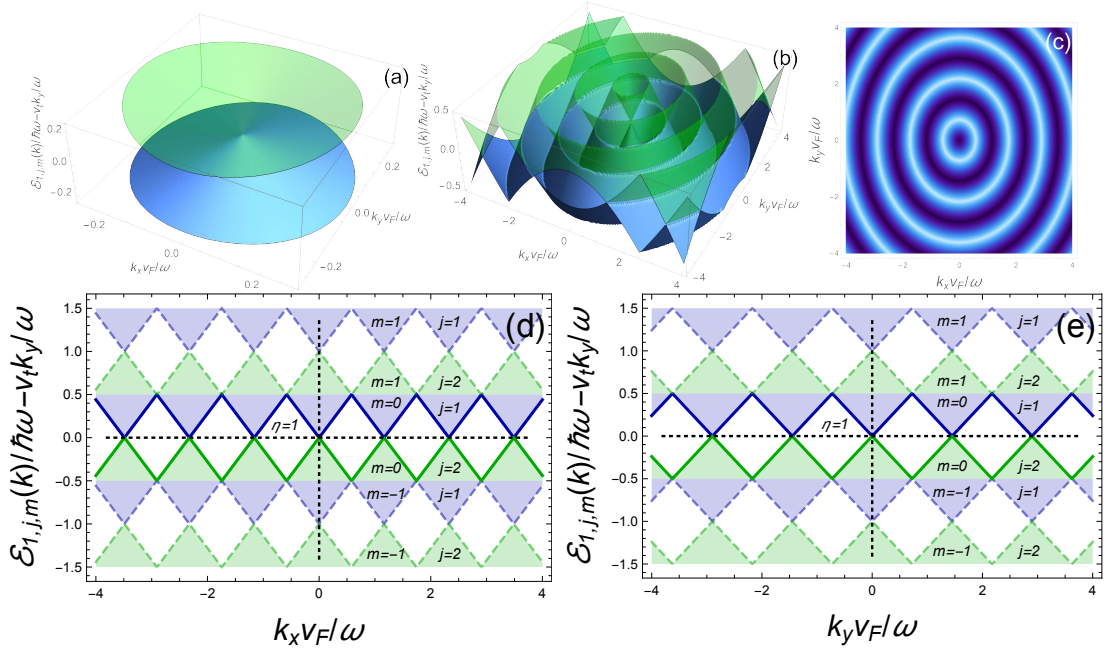
FIG. 1. Quasienergy-spectrum $\mathcal{E}_{\eta,j,m}(\boldsymbol{k}) - \hbar v_t k_y$ in the zero field regime ($E_x = E_y = 0$) for the K Dirac point $\eta = 1$; (a) Quasienergy spectrum as a function of the momentum components k_x and k_y in the vicinity of the Dirac point for the $j = 1$ (solid blue surface) and $j = 2$ (transparent green surface) bands. Only the first Floquet zone $m = 0$ is plotted. (b) Quasienergy-spectrum as a function of the momentum components k_x and k_y covering many different sections of the Dirac cone for the $j = 1$ (solid blue surface) and $j = 2$ (transparent green surface) bands. Only the first Floquet zone $m = 0$ is plotted. (c) Density plot of the quasienergy spectrum as a function of the momentum components k_x and k_y for the first band $j = 1$. (d) Quasienergy spectrum as a function of the momentum component k_x and fixed $k_y = 0$ for the $j = 1, 2$ bands (blue and green solid lines respectively) and the first three Floquet zones ($m = -1, 0, 1$). (e) Quasienergy spectrum as a function of the momentum component k_y and fixed $k_x = 0$ for the $j = 1, 2$ bands (blue and green solid lines respectively) and the first three Floquet zones ($m = -1, 0, 1$).

The time-dependent Schrödinger equation that arises from the Hamiltonian (5),

$$i\hbar \frac{\partial}{\partial t} \Psi(t, \boldsymbol{r}) = \mathcal{H}\Psi(t, \boldsymbol{r}), \qquad (8)$$

is easily solved by making the ansatz

$$\Psi(t, \boldsymbol{r}) = \exp(i\boldsymbol{k} \cdot \boldsymbol{r})\psi(t). \qquad (9)$$

This substitution considerably simplifies the problem by yielding the Schrödinger equation in $\boldsymbol{k}$-space

$$i\hbar \frac{d}{dt} \psi(t) = H(t)\psi(t), \qquad (10)$$

where the wave function $\psi(t)$ and the Hamiltonian

$$H(t) = v_t \left[\hbar k_y - eA_y(t)\right] \sigma_0$$
$$+ v_x \left[\hbar k_x - eA_x(t)\right] \sigma_x + v_y \left[\hbar k_y - eA_y(t)\right] \sigma_y, \qquad (11)$$

depend entirely on time.

Substituting the particular form of the vector potential

(6) into the Hamiltonian (11) gives

$$H(t) = v_t \left[\hbar k_y + e\frac{E_y}{\omega} \cos(\omega t + \phi)\right] \sigma_0$$
$$+ v_x \left[\hbar k_x + e\frac{E_x}{\omega} \cos(\omega t)\right] \sigma_x$$
$$+ v_y \left[\hbar k_y + e\frac{E_y}{\omega} \cos(\omega t + \phi)\right] \sigma_y. \qquad (12)$$

A simple inspection of this Hamiltonian reveals the limit between the strong and the weak field regimes. When the kinetic energy excels the radio frequency strength, $\hbar k > eE/\omega$ the system is in a weak field regime. Otherwise, it is in a strong field regime. In other words, the circle with radius

$$k = eE/\hbar\omega, \qquad (13)$$

is the boundary between the weak ($k > eE/\hbar\omega$) and strong field ($k < eE/\hbar\omega$) regions.
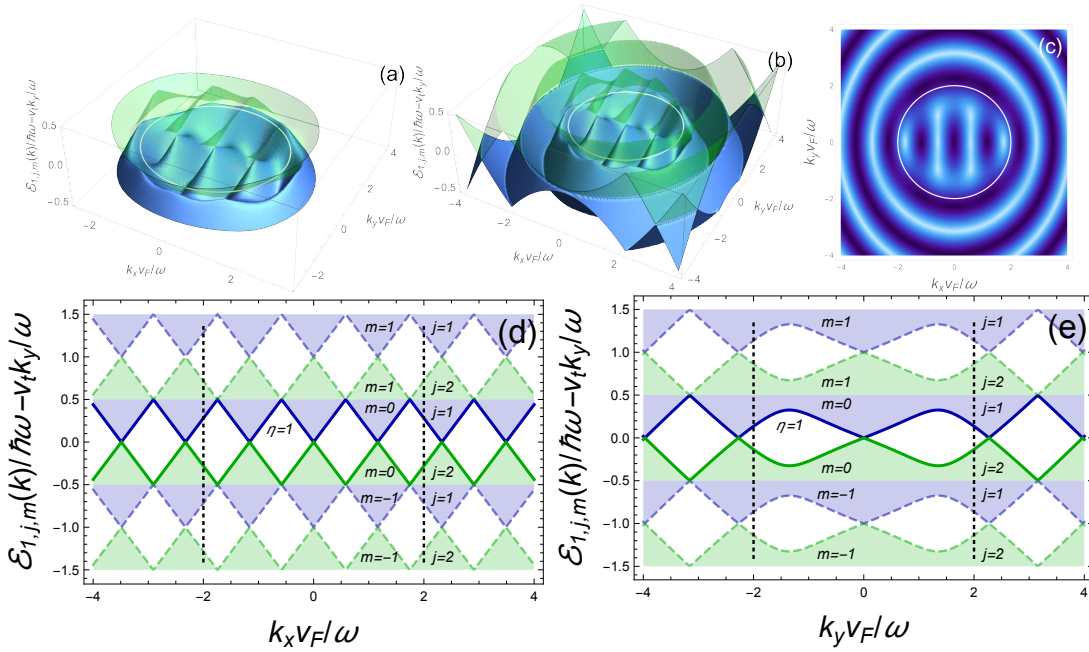
FIG. 2. Quasienergy-spectrum $\mathcal{E}_{\eta,j,m}(\boldsymbol{k}) - \hbar v_t k_y$ in the strong field regime for a linearly polarized wave ($E_x e v_F/\hbar\omega^2 = 2.0$, $E_y = 0$, $\phi = 0$) in the K Dirac point $\eta = 1$; (a) Quasienergy-spectrum as a function of the momentum components k_x and k_y for the $j = 1$ (solid blue surface) and $j = 2$ (transparent green surface) bands. Only the first Floquet zone $m = 0$ is plotted. A zoom of the original and two new Dirac points is shown. (b) Quasienergy-spectrum as a function of the momentum components k_x and k_y for the $j = 1$ (solid blue surface) and $j = 2$ (transparent green surface) bands. Only the first Floquet zone $m = 0$ is plotted. The wider range of $\boldsymbol{k}$ allows to see the three Dirac points emerging in the middle of the zero-field quasi-spectrum. (c) Density plot of the quasienergy-spectrum as a function of the momentum components k_x and k_y for the $j = 1$ band. (d) Quasienergy-spectrum as a function of the momentum component k_x and fixed $k_y = 0$ for the $j = 1, 2$ bands (blue and green solid lines respectively) and the first three Floquet zones ($m = -1, 0, 1$). (e) Quasienergy-spectrum as a function of the momentum component k_y and fixed $k_x = 0$ for the $j = 1, 2$ bands (blue and green solid lines respectively) and the first three Floquet zones ($m = -1, 0, 1$). The white curve in panels (a), (b) and (c) indicates the circle $k = eE/\hbar\omega = 2v_F/\omega$ that divides the strong ($k < eE/\hbar\omega$) and weak field regions ($k > eE/\hbar\omega$). The vertical dotted lines in panels (d) and (e) correspond to the position of edges of the circle $k = eE/\hbar\omega = \pm 2v_F/\omega$.

IV. TIME-EVOLUTION, QUASIENERGY-SPECTRUM AND THE MONODROMY MATRIX

Only a small number of very restrictive simple cases of Eq. (10) are exactly solvable. The most general and interesting cases are only approachable via numerical methods. The foregoing differential equation is usually addressed through the Floquet theorem and the subsequent Fourier time-frequency decomposition of the periodical part of the solution[36,45]. This approach trades the time-dependent differential equation (10) by an infinite-dimensional time-independent Hamiltonian matrix eigenvalue problem. This method presents two major drawbacks. First, to determine the quasienergy-spectrum through the diagonalization of the infinite-dimensional matrix it has to be chopped up to a required accuracy. The diagonalization process of such large matrices is of course numerical. Second, recovering the wave function in its spinor form requires the inverse Fourier transform of a very large dimensional eigenvector. Although this last step is not numerical, it relies in the numerically

obtained eigenvectors. Since the complexity of the problem presses for the use of numerical methods, instead, we compute the monodromy matrix from the numerical solution of the system of ordinary differential equations that stem from the Schrödinger equation. Conveniently, the quasi-states in the spinor form are a direct outcome of the previous calculation. The Schrödinger equation for the time evolution operator is[44]

$$i\hbar \frac{d}{dt}\mathcal{U}(t) = H(t)\mathcal{U}(t), \tag{14}$$

where $H(t)$ if given by (11), and $\mathcal{U}(t)$ is the time evolution operator. For the sake of simplicity, we set the initial condition $\mathcal{U}(0) = \mathbf{1}$ where $\mathbf{1}$ is the 2×2 identity matrix. Eq. (14) consists of four coupled scalar ordinary differential equations for the elements $U_{ij}(t)$ with initial conditions $U_{ij}(0) = \delta_{ij}$. Therefore, the solution of (14) encodes all the dynamical information of the system. Moreover, as a result of the Floquet theorem, the solution in any time interval can be extracted from the domain $t \in [0, T]$. Indeed, due to the periodicity of the Hamiltonian, $H(t) = H(t+T)$ where $T = 2\pi/\omega$, the evo-
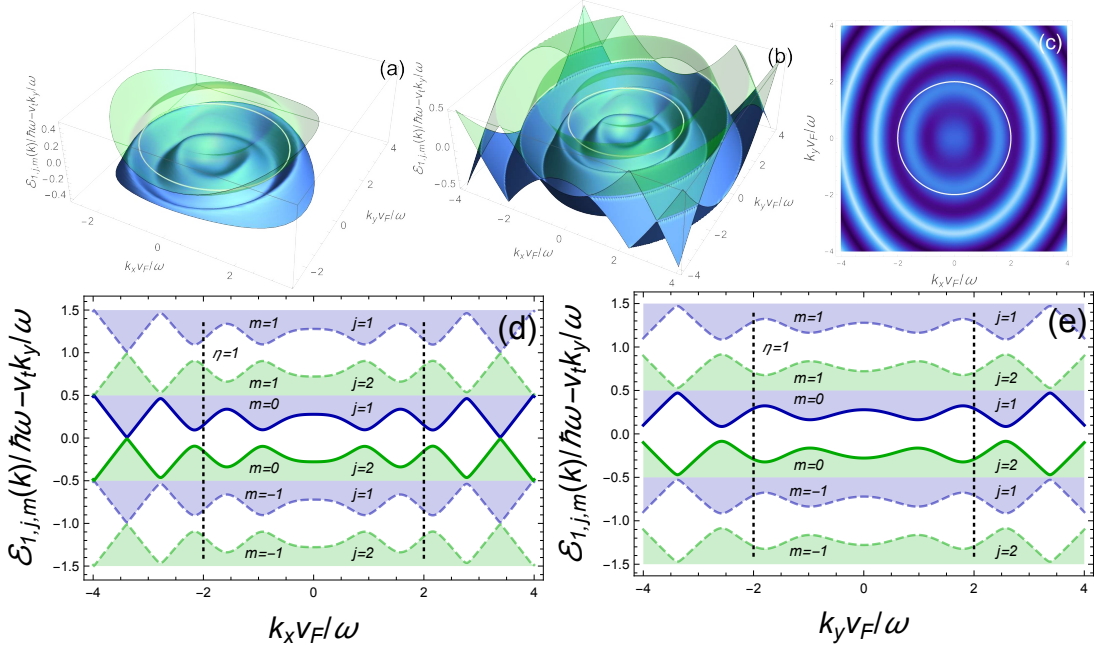
FIG. 3. Quasienergy-spectrum $\mathcal{E}_{\eta,j,m}(\boldsymbol{k}) - \hbar v_t k_y$ in the strong field regime for a circularly polarized wave ($E_x e v_F/\hbar\omega^2 = E_y e v_F/\hbar\omega^2 = \sqrt{2}$, $\phi = -\pi/2$) in the K Dirac point $\eta = 1$; (a) Quasienergy-spectrum as a function of the momentum components k_x and k_y for the $j = 1$ (solid blue surface) and $j = 2$ (transparent green surface) bands. Only the first Floquet zone $m = 0$ is plotted. (b) Quasienergy-spectrum as a function of the momentum components k_x and k_y for the $j = 1$ (solid blue surface) and $j = 2$ (transparent green surface) bands. Only the first Floquet zone $m = 0$ is plotted. The wider range of $\boldsymbol{k}$ allows to see the three Dirac points emerging in the middle of the zero-field quasi-spectrum. (c) Density plot of the quasienergy-spectrum as a function of the momentum components k_x and k_y for the $j = 1$ band. (d) Quasienergy-spectrum as a function of the momentum component k_x and fixed $k_y = 0$ for the $j = 1, 2$ bands (blue and green solid lines respectively) and the first three Floquet zones ($m = -1, 0, 1$). (e) Quasienergy-spectrum as a function of the momentum component k_y and fixed $k_x = 0$ for the $j = 1, 2$ bands (blue and green solid lines respectively) and the first three Floquet zones ($m = -1, 0, 1$). The white curve in panels (a), (b) and (c) indicates the circle $k = eE/\hbar\omega = 2v_F/\omega$ that divides the strong ($k < eE/\hbar\omega$) and weak field regions ($k > eE/\hbar\omega$). The vertical dotted lines in panels (d) and (e) correspond to the position of edges of the circle $k = eE/\hbar\omega = \pm 2v_F/\omega$.

lution operator must comply with the Floquet theorem. It states that[36,46]

$$\mathcal{U}(t) = \exp\left(-\frac{i}{\hbar}H_e t\right)\mathcal{W}(t), \qquad (15)$$

where $\mathcal{W}(t + T) = \mathcal{W}(t)$ and H_e is termed the effective Hamiltonian. The eigenvalues of H_e are precisely the quasienergies of $H(t)$. Thus, (15) allows us to compute the quasienergies and the time-dependent wave function $\psi(t)$ for $t \in [0, \infty)$ provided that the evolution operator is known in the interval $t \in [0, T]$. Let us assume that $U(t)$ is known in the domain $t \in [0, T]$, for example, through the numerical solution of Eq. (14), for a given set of k_x and k_y values. Since, by definition

$$\mathcal{U}(T) = \exp\left(-\frac{i}{\hbar}H_e T\right)\mathcal{W}(T) = \exp\left(-\frac{i}{\hbar}H_e T\right), \quad (16)$$

the quasienergies are given by

$$\mathcal{E}_{\eta,j,m}(\boldsymbol{k}) = -\frac{\hbar\omega}{2\pi}\arg[u_{\eta,j}(\boldsymbol{k})] + m\hbar\omega, \qquad (17)$$

where $u_{\eta,j}(\boldsymbol{k})$ are the two eigenvalues of $\mathcal{U}(T)$, and the subscripts $j = 1, 2$ and $m = 0, \pm 1, \pm 2, \ldots$ tag the band and the Floquet zone respectively. In the language of ordinary differential equations theory, $\mathcal{U}(T)$ is called the monodromy matrix[46,47], its eigenvalues $u_{\eta,j,\boldsymbol{k}}$ are named characteristic multipliers and $i\arg(u_{\eta,j,\boldsymbol{k}})/T$ are the characteristic exponents. Meanwhile, the evolution operator at any time is

$$\mathcal{U}(t) = \mathcal{W}(T)^{\lfloor t/T \rfloor}\mathcal{U}\left(\mathrm{mod}(t,T)\right), \qquad (18)$$

where $\lfloor t/T \rfloor = \mathrm{floor}(t/T)$.

V. RABI FORMULA

In many 2D materials, like graphene or borophene, the conduction and valence bands are symmetric with respect to the Fermi level. Thus, numerous similarities are shared with two-level systems[48]. In this section, we develop such analogy for the present model.

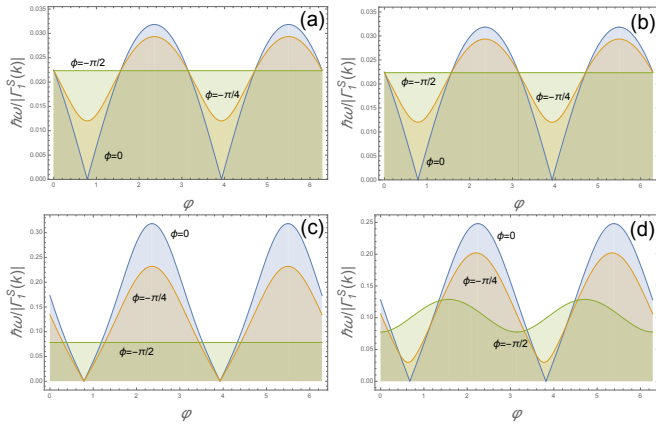In a two-level system, two important parameters ensue from the Rabi formula[44,49]: the detuning parameter

FIG. 4. Comparison of the single-photon mode transition time $\hbar\omega/\left|\Gamma_1^S(\boldsymbol{k})\right|$ as a function of the momentum direction given by the angle φ for graphene and borophene-like materials in the weak and strong-field regimes. (a) $v_t = 0$, $v_x = v_F$, $v_y = v_F$ (graphenel) and $E_x ev_F/\hbar\omega^2 = E_y ev_F/\hbar\omega^2 = 0.1/\sqrt{2}$ (weak-field regime); (b) $v_t = 0.32v_F$, $v_x = v_F$, $v_y = v_F$ (borophene) and $E_x ev_F/\hbar\omega^2 = E_y ev_F/\hbar\omega^2 = 0.1/\sqrt{2}$ (weak-field regime); (c) $v_t = 0$, $v_x = v_F$, $v_y = v_F$ (graphene) and $E_x ev_F/\hbar\omega^2 = E_y ev_F/\hbar\omega^2 = 1/\sqrt{2}$ (strong-field regime); (d) $v_t = 0.32v_F$, $v_x = v_F$, $v_y = v_F$ (borophene) and $E_x ev_F/\hbar\omega^2 = E_y ev_F/\hbar\omega^2 = 1/\sqrt{2}$ (strong-field regime). Three polarization cases are presented: $\phi = 0$ (linear polarization), $\phi = -\pi/2$ (circular polarization) and $\phi = -\pi/4$ (elliptical polarization).
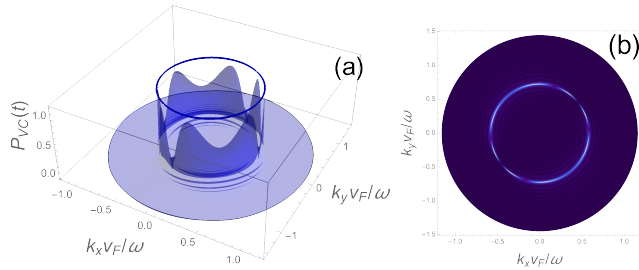

FIG. 5. (a) Three-dimensional and (b) density plots of the transition probability $P_{CV}(t)$ as a function of the momentum components k_x and k_y under linearly polarized light ($\phi = 0$) in the weak-field regime ($E_x ev_F/\hbar\omega^2 = E_y ev_F/\hbar\omega^2 = 0.01$). In panel (a) the solid dark blue elliptical line over the plot marks the zone where the single-photon resonant condition $2\epsilon(\boldsymbol{k}) = \hbar\omega$ is fulfilled.

Δ and the characteristic frequency Ω. The detuning parameter is a measure of how off is the field frequency from the quantum two-level system's resonant frequency. When the field is tuned to the resonant frequency, i.e. $\Delta = 0$, the system is capable of transitioning from one-level to the other with probability equal to 1 after a certain time. In contrast, when $\Delta \neq 0$, the system will at best reach a superposition of both states. The change rate from one state to the other is given by the characteristic frequency: a fourth of its period $\tau = \pi/2\Omega$ is the time elapsed between the start and the completion of the
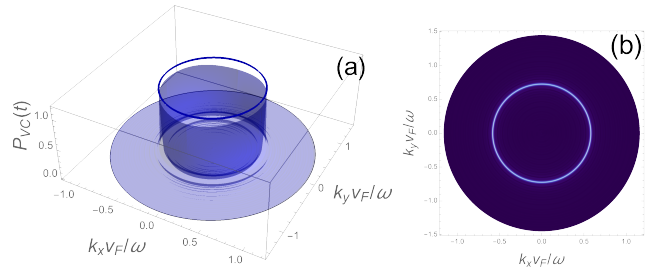

FIG. 6. (a) Three-dimensional and (b) density plots of the transition probability $P_{CV}(t)$ as a function of the momentum components $k_{x,y}$ under circularly polarized light ($\phi = -\pi/2$) in the weak-field regime ($E_x ev_F/\hbar\omega^2 = E_y ev_F/\hbar\omega^2 = 0.01$). In panel (a) the solid dark blue elliptical line over the plot marks the zone where the single-photon resonant condition $2\epsilon(\boldsymbol{k}) = \hbar\omega$ is fulfilled.
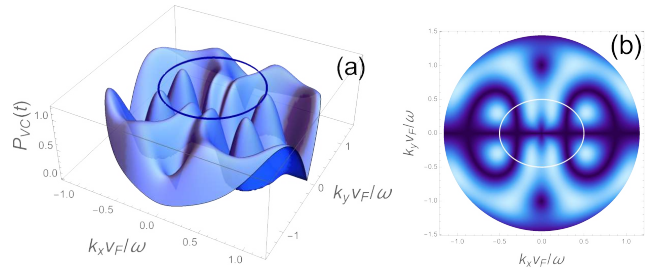

FIG. 7. (a) Three-dimensional and (b) density plots of the transition probability $P_{CV}(t)$ as a function of the momentum components $k_{x,y}$ under linearly polarized light ($\phi = 0$) in the strong-field regime ($E_x ev_F/\hbar\omega^2 = 1, E_y ev_F/\hbar\omega^2 = 0$). The solid dark blue (a) and white (b) elliptical lines mark the zone where the single-photon resonant condition $2\epsilon(\boldsymbol{k}) = \hbar\omega$ is fulfilled.

quantum transition[44]. Even though, it is usually proportional to the quantum system-radiation interaction strength, we will see further on that the added complexity of 2D Dirac materials yields a considerably richer and more intricate behaviour.

Our main goal is now to identify these two Rabi parameters from the Schrödinger equation (10). This will allow us to predict the conditions for producing Rabi cycles and their duration. We follow a three stage strategy in which we first move to the conduction-valence band basis, then remove the time-dependent diagonal elements of the Hamiltonian and finally adopt the rotating wave approximation. This procedure requires a total of four unitary transformations.

In the case studied here, the two-state quantum system is embodied by the conduction and valence band states at a given momentum state of the 2D Dirac material. In particular, we are concerned with the field stimulated transitions that occur between the valence and conduction band. Therefore, as a starting point, we wish to express the Hamiltonian (11) in the basis of the valence and conduction band states (2). To this end let us act
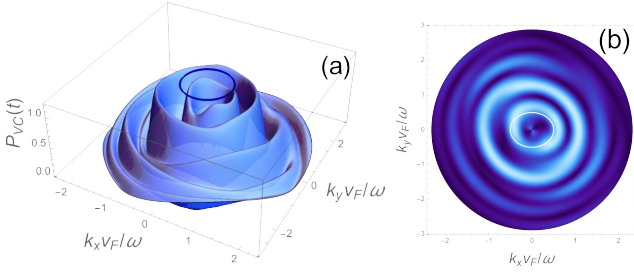
FIG. 8. (a) Three-dimensional and (b) density plots of the transition probability $P_{CV}(t)$ as a function of the momentum components $k_{x,y}$ under circularly polarized light ($\phi = -\pi/2$) in the strong-field regime ($E_x ev_F/\hbar\omega^2 = E_y ev_F/\hbar\omega^2 = 1/\sqrt{2}$). The solid dark blue (a) and white (b) elliptical lines mark the zone where the single-photon resonant condition $2\epsilon(\boldsymbol{k}) = \hbar\omega$ is fulfilled.

(10) by the first unitary transformation

$$
\begin{aligned}
\mathcal{R}_1 &= \frac{1}{\sqrt{2}} \begin{pmatrix} 1 & 1 \\ e^{i\theta(\boldsymbol{k})} & -e^{i\theta(\boldsymbol{k})} \end{pmatrix} \\
&= \frac{e^{i\theta(\boldsymbol{k})/2}}{\sqrt{2}} \left\{ \cos\left[\frac{\theta(\boldsymbol{k})}{2}\right] (\sigma_x + \sigma_z) \right. \\
&\quad \left. + \sin\left[\frac{\theta(\boldsymbol{k})}{2}\right] (\sigma_y - i\sigma_0) \right\}. \quad (19)
\end{aligned}
$$

The Schrödinger equation for the transformed evolution operator $U = \mathcal{R}_1^\dagger \mathcal{U}(t)\mathcal{R}$ in the conduction and valence band base takes the form

$$
\begin{aligned}
0 &= \mathcal{R}_1^\dagger \left[i\hbar\frac{d}{dt} - H(t)\right] \mathcal{U}(t)\mathcal{R}_1 \\
&= \left\{ i\hbar\frac{d}{dt} - [\gamma(\boldsymbol{k}) + \lambda(\boldsymbol{k})\cos(\omega t + \phi)]\sigma_0 \right. \\
&\quad - [\epsilon(\boldsymbol{k}) + \alpha(\boldsymbol{k})\cos(\omega t) + \beta(\boldsymbol{k})\cos(\omega t + \phi)]\sigma_z \\
&\quad \left. - i[\mu(\boldsymbol{k})\cos(\omega t) - \nu(\boldsymbol{k})\cos(\omega t + \phi)](\sigma_+ - \sigma_-) \right\} U(t),
\end{aligned}
$$
$$(20)$$

where the spin ladder operators are defined by

$$
\sigma_+ = \frac{\sigma_x + i\sigma_y}{2}, \quad (21)
$$

$$
\sigma_- = \frac{\sigma_x - i\sigma_y}{2}, \quad (22)
$$

the $\boldsymbol{k}$-dependent coefficients as,

$$
\alpha(\boldsymbol{k}) = \hbar\frac{v_x^2 k_x e E_x}{\omega\epsilon(\boldsymbol{k})}, \quad (23)
$$

$$
\beta(\boldsymbol{k}) = \hbar\frac{v_y^2 k_y e E_y}{\omega\epsilon(\boldsymbol{k})}, \quad (24)
$$

$$
\gamma(\boldsymbol{k}) = \hbar v_t k_y, \quad (25)
$$

$$
\lambda(\boldsymbol{k}) = \frac{v_t e E_y}{\omega}, \quad (26)
$$

$$
\mu(\boldsymbol{k}) = \hbar\frac{v_x v_y k_y e E_x}{\omega\epsilon(\boldsymbol{k})}, \quad (27)
$$

$$
\nu(\boldsymbol{k}) = \hbar\frac{v_x v_y k_x e E_y}{\omega\epsilon(\boldsymbol{k})}, \quad (28)
$$

and $\epsilon(\boldsymbol{k})$ is given by (4). The next two transformations are devoted to eliminating the time-dependent elements in the diagonal of the Schrödinger equation. First, we remove the terms proportional to σ_0 by means of applying

$$
\mathcal{R}_2 = \exp\left[-\frac{i}{\hbar}\Xi(\boldsymbol{k},t)\sigma_0\right]. \quad (29)
$$

where $\alpha(\boldsymbol{k})$ and $\beta(\boldsymbol{k})$ have been absorbed in the complex number

$$
\Xi(\boldsymbol{k},t) = \gamma(\boldsymbol{k})t + \frac{\lambda(\boldsymbol{k})}{\omega}[\sin(\omega t + \phi) - \sin(\phi)]. \quad (30)
$$

Under this transformation, the Schrödinger equation becomes

$$
\begin{aligned}
0 &= \mathcal{R}_2^\dagger \left[i\hbar\frac{d}{dt} - H(t)\right] U(t)\mathcal{R}_2 \\
&= \left\{ i\hbar\frac{d}{dt} - [\epsilon(\boldsymbol{k}) + \alpha(\boldsymbol{k})\cos(\omega t) + \beta(\boldsymbol{k})\cos(\omega t + \phi)]\sigma_z \right. \\
&\quad - i[\mu(\boldsymbol{k})\cos(\omega t) - \nu(\boldsymbol{k})\cos(\omega t + \phi)] \\
&\quad \left. \times (\sigma_+ - \sigma_-) \right\} U_2(t), \quad (31)
\end{aligned}
$$

where $U_2(t) = \mathcal{R}_2^\dagger U(t)\mathcal{R}_2$. In a similar way, the following transformation lifts the time-dependence from the entries proportional to σ_z. This transformation is given by the following rotation around the z axis

$$
\mathcal{R}_3 = \exp\left[-\frac{i}{\hbar}\Lambda(\boldsymbol{k},t)\sigma_z\right]. \quad (32)
$$

The time-dependent transformation parameter is given by

$$
\begin{aligned}
\Lambda(\boldsymbol{k},t) &= \frac{1}{\omega}\left[\alpha(\boldsymbol{k})\sin(\omega t) \right. \\
&\quad \left. + \beta(\boldsymbol{k})\sin(\omega t + \phi) - \beta(\boldsymbol{k})\sin(\phi)\right] \\
&= \frac{\chi(\boldsymbol{k})}{\omega}\cos(\omega t + \zeta(\boldsymbol{k})) - \frac{\beta(\boldsymbol{k})}{\omega}\sin(\phi), \quad (33)
\end{aligned}
$$

where

$$\chi(\boldsymbol{k})\mathrm{e}^{i\zeta(\boldsymbol{k})} = \frac{\alpha(\boldsymbol{k}) + \beta(\boldsymbol{k})\mathrm{e}^{i\phi}}{i}. \quad (34)$$

The reduced Schrödinger equation takes the form

$$0 = \mathcal{R}_3^\dagger \mathcal{R}_2^\dagger \left[i\hbar \frac{d}{dt} - H(t) \right] U(t)\mathcal{R}_2\mathcal{R}_3$$

$$= \left[i\hbar \frac{d}{dt} - \epsilon(\boldsymbol{k})\sigma_z \right.$$

$$\left. + \Gamma(\boldsymbol{k},t)\sigma_+ + \Gamma^*(\boldsymbol{k},t)\sigma_- \right] U_3(t), \quad (35)$$

where the transformed evolution operator is $U_3(t) = \mathcal{R}_3^\dagger \mathcal{R}_2^\dagger U(t)\mathcal{R}_2\mathcal{R}_3$ and

$$\Gamma(\boldsymbol{k},t) = -\frac{i}{2}\left[\mu(\boldsymbol{k})\cos(\omega t) + \nu(\boldsymbol{k})\cos(\omega t + \phi) \right]$$

$$\times \exp\left[-\frac{2i\Lambda(\boldsymbol{k},t)}{\hbar} \right]. \quad (36)$$

At this stage, the Schrödinger equation takes the more familiar form where the diagonal elements (proportional to σ_z) are constant and the time-dependent ones are secluded to the off-diagonal entries (proportional to σ_+ and σ_-). We can, therefore, move on to the rotating wave approximation[50]. It consists in setting the system in a rotating frame that revolves around the z axis at an angular velocity ω keeping the constant terms and discarding those that rapidly oscillate[50]. In the standard analysis of Rabi oscillations, the radio frequency field may be decomposed into the two circular components. One rotates in the same direction as the rotating frame and the other in the opposite direction[51]. While the component rotating synchronously with the frame becomes constant, the other rapidly oscillates at an angular frequency 2ω. The last one is neglected as it is quickly averaged over time yielding an approximated constant Hamiltonian. This approximation is justified as long as the static field is larger than the oscillating one[51].

In our case, however, a fundamental difference surfaces when we look closely at the parameter $\Gamma(\boldsymbol{k},t)$. Using the Jacobi-Anger expansion

$$\exp(iz\cos\varphi) = \sum_{n=-\infty}^{\infty} i^n J_n(z)\exp(in\varphi), \quad (37)$$

we obtain the following Fourier series:

$$\Gamma(\boldsymbol{k},t) = \frac{i}{2}\exp\left[-\frac{2i\beta(\boldsymbol{k})}{\hbar\omega}\sin\phi \right]$$

$$\times \sum_{n=-\infty}^{\infty} i^n \exp\left[in\zeta(\boldsymbol{k}) \right] J_n\left[\frac{2\chi(\boldsymbol{k})}{\hbar\omega} \right]$$

$$\times \left\{ \left[\nu(\boldsymbol{k})\mathrm{e}^{i\phi} - \mu(\boldsymbol{k}) \right] \exp\left[i(n+1)(\omega t + \delta) \right] \right.$$

$$\left. + \left[\nu(\boldsymbol{k})\mathrm{e}^{-i\phi} - \mu(\boldsymbol{k}) \right] \exp\left[i(n-1)(\omega t + \delta) \right] \right\}, \quad (38)$$

where in the previous expression we have restored the initial field phase δ.

In contrast with the classical treatment of Rabi oscillations, where only one oscillating mode is present, here, the Hamiltonian is composed of an infinite number of Fourier modes. This is our first evidence as to why multi-photon modes are generated in Dirac materials while in standard Rabi systems only the single-photon one is present. We can nevertheless follow the usual prescription of the rotating wave approximation with a slight modification. Rotating around the z axis by a phase $-q\omega t$, where $q \in \mathbb{Z}$, we tune in with each one of the Fourier modes. This is accomplished through the rotation operator

$$\mathcal{R}_4 = \exp\left(-\frac{i}{2}q\omega t\sigma_z \right). \quad (39)$$

In the rotating frame the Schrödinger equation (35) takes the form

$$0 = \mathcal{R}_4^\dagger \mathcal{R}_3^\dagger \mathcal{R}_2^\dagger \mathcal{R}_1^\dagger \left[i\hbar \frac{d}{dt} - H(t) \right] U(t)\mathcal{R}_1\mathcal{R}_2\mathcal{R}_3\mathcal{R}_4$$

$$= \left\{ i\hbar \frac{d}{dt} - \left[\epsilon(\boldsymbol{k}) - \frac{q\hbar\omega}{2} \right]\sigma_z \right.$$

$$\left. + \Gamma(\boldsymbol{k},t)\mathrm{e}^{iq\omega t}\sigma_+ + \Gamma^*(\boldsymbol{k},t)\mathrm{e}^{-iq\omega t}\sigma_- \right\} U_4(t). \quad (40)$$

where, as before, the transformed evolution operator is

$$U_4(t) = \mathcal{R}_4^\dagger \mathcal{R}_3^\dagger \mathcal{R}_2^\dagger U(t)\mathcal{R}_2\mathcal{R}_3\mathcal{R}_4. \quad (41)$$

By the Fourier expansion (38) we readily identify the synchronous terms

$$\Gamma_q^S(\boldsymbol{k}) = \frac{i^q}{2}\mathrm{e}^{-iq[\delta+\zeta(\boldsymbol{k})]}\exp\left[-\frac{2i\beta(\boldsymbol{k})}{\hbar\omega}\sin\phi \right]$$

$$\times \left\{ \mathrm{e}^{i\zeta(\boldsymbol{k})} J_{q-1}\left[\frac{2\chi(\boldsymbol{k})}{\hbar\omega} \right] \left[\nu(\boldsymbol{k})\mathrm{e}^{-i\phi} - \mu(\boldsymbol{k}) \right] \right.$$

$$\left. - \mathrm{e}^{-i\zeta(\boldsymbol{k})} J_{q+1}\left[\frac{2\chi(\boldsymbol{k})}{\hbar\omega} \right] \left[\nu(\boldsymbol{k})\mathrm{e}^{i\phi} - \mu(\boldsymbol{k}) \right] \right\}. \quad (42)$$

Neglecting all the components rotating with higher frequencies, we end up with a static equation,

$$0 = \left\{ i\hbar \frac{d}{dt} - \left[\epsilon(\boldsymbol{k}) - \frac{q\hbar\omega}{2} \right]\sigma_z \right.$$

$$\left. + \Gamma_q^S(\boldsymbol{k})\sigma_+ + \Gamma_q^{S*}(\boldsymbol{k})\sigma_- \right\} U_4(t). \quad (43)$$

In order for this approximation to be valid, the static entries $[\epsilon(\boldsymbol{k})]$ must be larger than the oscillating ones $[\Gamma_q^S(\boldsymbol{k})]$, thus

$$\epsilon(\boldsymbol{k}) \gg \left| \Gamma_q^S(\boldsymbol{k}) \right|. \quad (44)$$

The formal solution of (43) is

$$
\begin{aligned}
U_4(t) = \exp\Bigg\{ & \frac{it}{\hbar}\left[\epsilon(\boldsymbol{k}) - \frac{q\hbar\omega}{2}\right]\sigma_z \\
& - \frac{it}{\hbar}\left[\Gamma_q^S(\boldsymbol{k})\sigma_+ + \Gamma_q^{S*}(\boldsymbol{k})\sigma_-\right]\Bigg\} \\
= & \cos[\Omega_q(\boldsymbol{k})t]\sigma_0 + \frac{i}{\hbar\Omega_q(\boldsymbol{k})}\sin[\Omega_q(\boldsymbol{k})t] \\
& \times \left[\Delta_q(\boldsymbol{k})\sigma_z - \Gamma_q^S(\boldsymbol{k})\sigma_+ - \Gamma_q^{S*}(\boldsymbol{k})\sigma_-\right], \quad (45)
\end{aligned}
$$

where

$$
\Delta_q(\boldsymbol{k}) = \epsilon(\boldsymbol{k}) - \frac{q\hbar\omega}{2}, \tag{46}
$$

$$
\Omega_q(\boldsymbol{k}) = \frac{1}{\hbar}\sqrt{\Delta_q^2(\boldsymbol{k}) + \left|\Gamma_q^S(\boldsymbol{k})\right|^2}, \tag{47}
$$

As one of the last steps, we have to work back the solution for the actual evolution operator from (41)

$$
\begin{aligned}
U(t) = & \mathcal{R}_2\mathcal{R}_3\mathcal{R}_4 U_4(t)\mathcal{R}_4^\dagger\mathcal{R}_3^\dagger\mathcal{R}_2^\dagger \\
= & \cos[\Omega_q(\boldsymbol{k})t]\sigma_0 + \frac{i}{\hbar\Omega_q(\boldsymbol{k})}\sin[\Omega_q(\boldsymbol{k})t] \\
\times \Bigg\{ & \Delta_q(\boldsymbol{k})\sigma_z - \exp\left[-\frac{2i\Lambda(\boldsymbol{k},t)}{\hbar} - iq\omega t\right]\Gamma_q^S(\boldsymbol{k})\sigma_+ \\
& - \exp\left[\frac{2i\Lambda(\boldsymbol{k},t)}{\hbar} + iq\omega t\right]\Gamma_q^{S*}(\boldsymbol{k})\sigma_-\Bigg\}. \quad (48)
\end{aligned}
$$

Finally, the probability of transitioning from the conduction to the valence band is

$$
P_{CV}(t) = \left|\psi_V^\dagger U(t)\psi_C\right|^2 = \frac{\left|\Gamma_q^S(\boldsymbol{k})\right|^2}{\left[\hbar\Omega_q(\boldsymbol{k})\right]^2}\sin^2\left[\Omega_q^2(\boldsymbol{k})t\right], \tag{49}
$$

where, in the conduction-valence band base we have

$$
\psi_C = (1,0)^\top, \qquad \psi_V = (0,1)^\top. \tag{50}
$$

Equation (49) is the Rabi equation. From it we can infer that the detuning parameter is $\Delta_q(\boldsymbol{k}) = \epsilon(\boldsymbol{k}) - q\hbar\omega/2$. It is hardly surprising that the maximum transition probability amplitude is attained when $\Delta_q(\boldsymbol{k}) = 0$ or equivalently when $\Omega_q(\boldsymbol{k}) = |\Gamma_q^S(\boldsymbol{k})|$. This simply means that, in the $k_x - k_y$ plane, full transitions between the valence and conduction bands may occur between points having the same $\boldsymbol{k}$ values and whose energy difference complies with

$$
2\epsilon(\boldsymbol{k}) = q\hbar\omega. \tag{51}
$$

We call this the resonance condition. One can thus picture electron transitions as occurring vertically from one ellipse in the valence band to another one in the conduction band.

The truly significant behaviours arise from the convoluted structure of the transition time

$$
\tau_q(\boldsymbol{k}) = \frac{\pi\hbar}{2\sqrt{\left[\epsilon(\boldsymbol{k}) - \frac{q\hbar\omega}{2}\right]^2 + \left|\Gamma_q^S(\boldsymbol{k})\right|^2}}. \tag{52}
$$

Despite the highly symmetrical condition imposed by the detuning parameter, the transition time is able to introduce a high degree of anisotropy as we will show later on. If the resonance condition (51) is met

$$
\tau_q(\boldsymbol{k}) = \frac{\pi\hbar}{\left|\Gamma_q^S(\boldsymbol{k})\right|}. \tag{53}
$$

This relation deserves special attention since it establishes a connection between the intensity of the electric field and multi-photon processes. When the rotating frame synchronizes with the ω ($q = 1$) mode, one of the terms of $\Gamma_q^S(\boldsymbol{k})$ is proportional to the Bessel function of zeroth order $J_0[2\chi(\boldsymbol{k})/\hbar\omega]$. This is the only integer order Bessel function that does not vanish upon being evaluated at zero. Since $\chi(\boldsymbol{k})$ is proportional to the magnitude of the electric field, $|\Gamma_1^S(\boldsymbol{k})|$ ($q = 1$) is the dominant synchronous entry in Eq. (40) for low electromagnetic fields. As the intensity of the electromagnetic field rises, it activates synchronous terms with larger q that involve more photon interactions. These are proportional to Bessel functions of higher order that vanish when evaluated at zero, and therefore come in to play for large values of the amplitude of the electric field. In virtue of the resonance condition (51), a high intensity light pulse might hit multi-photon resonances ($q > 1$) aside from the single-photon one, that is always triggered regardless of the field strength.

VI. NUMERICAL RESULTS

The quasienergies of Hamiltonian (11) are computed through Eq. (17). By numerically solving the four differential equations that arise from (14), the evolution operator $\mathcal{U}(t)$ matrix elements are determined in the time interval $t \in [0, T]$. These, in turn, are used to compute the eigenvalues $u_{\eta,j}(\boldsymbol{k})$ of $\mathcal{U}(T)$ that enter Eq. (17). Through these calculations, we have analyzed three cases: vanishing, linearly polarized and circularly polarized intense fields.

Figure 1 shows the zero-field quasi-spectrum. For the sake of simplicity, in this figure and the ones that follow we have removed the tilting by plotting $\Gamma_q^S(\boldsymbol{k}) - \hbar v_t k_y$. Although most readers familiar with Dirac materials and Floquet theory will immediately recognize the zero-field quasi-spectrum in this figure, it is worthwhile reviewing it in order to be able to make a proper comparison with the two other cases. If the field vanishes one can either obtain the energy or the quasienergy-spectrum given that, under such conditions, the Hamiltonian is time-independent. However, when a periodical time-varying electromagnetic field is present, the notion of energy is rendered meaningless and we can only speak of quasienergies. Even though the energy spectrum in vanisghing fields is widely known, the quasienergy requires some further consideration. It is comprised of two valence and conduction band cones whose tips touch in the Dirac point as can be seen in Fig. (1) (a) . Both cones extend to infinity in opposite

directions in $\boldsymbol{k}$-space. By definition, the quasienergy is a phase and, as such, it is only unambiguously defined in $0 \leq \mathcal{E}_{\eta,j,m}(\boldsymbol{k}) \leq \hbar\omega$. Any quasienergy value lying outside will thus be echoed in the same range. As we mentioned earlier, we call this range Floquet zone. These repetitions are clearly seen in Fig. 1 (b) where the quasienergy spectrum is plotted as a function of the momentum components $k_{x,y}$ for zero-field case. The two bands $j = 1$ (transparent green) and $j = 2$ (solid blue) of the first Floquet band ($m = 0$) are shown in Fig. 1 (a). We readily spot the tips of both bands' Dirac cones touching in $k_x = k_y = 0$. As both cones extend and reach the edges of the Floquet zone, they reemerge in the opposite side as part of the other band ($m = 1 \rightarrow m = 2$ or $m = 2 \rightarrow m = 1$). In this manner, the multiple sections of the Dirac cone are arranged concentrically around the tip of the Dirac cone. Panel (c) shows the quasi-spectrum density plot. The Dirac point is located in the center of the dark elliptical zone ($k_x = k_y = 0$) and the contours of the cylindrical sections that reach the upper boundary of the Floquet zone are depicted as bright lines. Figures (1) (d) and (e) show cross sections of the quasienergy for $k_y = 0$ and $k_x = 0$ respectively. In these figures we clearly see the multiple sections of the cones switching from one band to the other as they cross from one Floquet zone ($m = -1, 0, 1$) to the next.

The effects of an linearly polarized electromagnetic field in the quasienergy-spectrum as a function of the momentum components k_x and k_y can be viewed in Fig. 2. The polarization of the electromagnetic field is along the x direction ($E_x = 2\hbar\omega^2/ev_F$ and $Ey = 0$). In panel (a) we have plotted the quasienergies of the two bands ($j = 1$ and $j = 2$). In panel (b) we can appreciate further details in the quasienergy density plot of the first band ($j = 1$). We immediately notice a striking difference with the zero field quasi-spectrum: the concentric circles are replaced by a grid pattern. The grid lines are oriented along the direction perpendicular to the field polarization and a complex pattern of new Dirac-like points emerges around the original one. The quasienergy spectrum cross sections at $k_y = 0$ and $k_x = 0$ are shown in panels (d) and (e). While the $k_y = 0$ cross section seems unaltered by the presence of the electromagnetic radiation, the quasi-spectrum is significantly elongated in the $k_x = 0$ projection. This can be attributed to a renormalization of the material parameters, mainly the v_x and v_y velocities in the vicinity of the original Dirac point an the newly formed ones. The deformation of the spectrum may be understood as the result of electronic dressing[31]. It is important to underline that, even though the spectrum has been considerably deformed, the original Dirac point is preserved under the action of a linearly polarized field. This same behaviour has been observed by us by a completely different mathematical approach that relies in the Fourier spectral decomposition of the wave function[33].

The boundary between the weak ($k > eE/\hbar\omega$) and strong field ($k < eE/\hbar\omega$) regimes is indicated with a solid white line in Figs. (2) (a), (b) and (c). In Figs.

(2) (d) and (e) the edges of the circle are marked vertical dotted black lines. It can be seen that the deformation of the quasienergy-spectrum with respect to the zero field case is always restricted to the strong field region.

Figure 3 exhibits the quasienergy-spectrum under a circularly polarized illumination. The fundamental difference with the spectrum of linearly polarized radiation is that for circularly polarized light a Gap opens up in the Dirac point. Similarly as under linearly polarized light, the spectrum is strongly distorted within the strong field region $k < eE/\hbar\omega$, however, the distortion has cylindrical symmetry. In the same manner as for the linearly polarized field, in Figs. 3 (a), (b) and (c) the white circle indicates the boundary between the strong and the weak field regimes. Likewise, in Figs. 3 (d) and (e) the vertical dotted black lines mark the edges between both regions.

VII. DISCUSSION

Now we would like to establish a link between the structure of the spectrum and the transition probability under pulsed illumination. Before proceeding further, it is instructive to examine the behaviour of the transition time $\pi\hbar/\left|\Gamma_1^S(\boldsymbol{k})\right|$ subject to a resonant field ($\hbar\omega = 2\epsilon(\boldsymbol{k})$). A suitable parametrization of the momentum vector under these conditions is

$$\boldsymbol{k} = \frac{\omega}{2v_x}\cos\varphi\hat{\boldsymbol{\imath}} + \frac{\omega}{2v_y}\sin\varphi\hat{\boldsymbol{\jmath}}, \qquad (54)$$

where the parameter φ is a directional angle in the $k_x - k_y$-plane. Figure 4 presents plots of the single-photon mode transition time $\pi\hbar/|\Gamma_1^S(\boldsymbol{k})|$ as a function of the parameter φ for graphene ($v_t = 0$ and $v_x = v_y$) [(a) and (c)] and borophene-like ($v_t \neq 0$ and $v_x \neq v_y$) [(b) and (d)] materials submitted to weak and strong fields. The rotational symmetry of graphene provides a reference point to discriminate if the transition time behaviour originates in the anisotropic velocities or the field polarization. In these figures we can appreciate that while circularly polarized light has no directional effects, in highly symmetrical materials, linearly polarized field consistently exhibits variations in the transition time regardless of the field intensity. We also infer that small variations of the transition time are expected for anisotropic materials under circularly polarized illumination. Much larger fluctuations are, however, expected under linearly polarized light.

Having examined the behaviour of the resonant transition time we now turn to the analysis of the transition probability of carriers under a pulsed light excitation. To this end we use the vector potential of a square pulse

$$\boldsymbol{A}(t) = -\frac{E_x}{\omega}\cos\left(\omega t + \delta\right)\Theta[\tau_1(\boldsymbol{k}), t - t_0]\hat{\boldsymbol{\imath}}$$
$$- \frac{E_y}{\omega}\cos\left(\omega t + \delta + \phi\right)\Theta[\tau_1(\boldsymbol{k}), t - t_0]\hat{\boldsymbol{\jmath}}, \quad (55)$$

where the step function is defined as

$$\Theta[\tau_1(\boldsymbol{k}), t] = \begin{cases} 1, \ 0 \leq t \leq \tau_1(\boldsymbol{k}), \\ 0, \ 0 > t > \tau_1(\boldsymbol{k}). \end{cases} \tag{56}$$

Plugging this expression for the vector potential into the Schrödinger equation (14) and numerically calculating the evolution operator $\mathcal{U}(t)$ we readily obtain the transition probability

$$P_{CV}(t) = \left| \psi_C^\dagger \, \mathcal{U}(t) \, \psi_V \right|^2 , \tag{57}$$

where the valence and conduction band states are expressed in the sublattice state basis as

$$\psi_V = \frac{1}{\sqrt{2}} \left(1, -e^{i\theta(\boldsymbol{k})} \right)^\top , \quad \psi_C = \frac{1}{\sqrt{2}} \left(1, e^{i\theta(\boldsymbol{k})} \right)^\top . \tag{58}$$

The duration of the pulse matches the single-photon resonant transition time $\tau_{1,\boldsymbol{k}}$ for a momentum state characterized by $\boldsymbol{k}$. After the pulse, the wave function of the system will reach a steady state if it is allowed to evolve for a sufficiently long time $t > t_0 + \tau_{1,\boldsymbol{k}}$. One would expect that such a pulse will induce a full transition ($P_{CV} = 1$) between the valence ψ_V and the conduction ψ_C band states provided that their energy difference matches the resonant condition $2\epsilon(\boldsymbol{k}) = \hbar\omega$. While this is true in the weak-field regime, the strong-field regime presents a far more complex behaviour.

Figure 5 shows plots of $P_{CV}[t > t_0 + \tau_1(\boldsymbol{k})]$ as a function of k_x and k_y for a linearly polarized field ($\phi = 0$) in the weak field regime ($E_x ev_F/\hbar\omega^2 = E_y ev_F/\hbar\omega^2 = 0.01$). We clearly observe that transitions are strictly confined to the $\boldsymbol{k}$-space region where the resonant condition $2\epsilon(\boldsymbol{k}) = \hbar\omega$ is met. In panel (a) this region is indicated by the elliptical solid line above the plot. Furthermore, along this line the probability is not uniform and is oriented in accord with the electric field direction. The density plot in panel (b) shows a vanishing probability along the polarization line. Given that the resonant condition is perfectly elliptical, this asymmetry is rather attributed to the anisotropies of the transition time.

Unlike linearly polarized light, circularly polarized light ($\phi = -\pi/2$, $E_x ev_F/\hbar\omega^2 = E_y ev_F/\hbar\omega^2 = 0.01$) produces a largely even transition probability as can be seen in Fig. 6. As expected, full transitions occur only where the resonant condition is fulfilled as suggested by the consistency between P_{CV} and the solid elliptical line above the plot in panel (a). Though not visible in panel (b), smooth variations of the probability are noticeable close to $P_{CV} = 1$ in panel (a). As we discussed above, these small changes in P_{CV} are due to the fluctuations of the transition time as a function of $\boldsymbol{k}$. These in turn are due to the anisotropic velocities v_x and v_y.

The transition probability as a function of k_x and k_y exhibits completely different features in the strong field regime. Figures 7 and 8 present $P_{CV}(t)$ plots alike those in Figs. 5 and 6, but in the strong field regime. A common feature to both polarizations is that a pulse of given frequency ω and duration $\tau_{1,\boldsymbol{k}}$ is capable of exciting states that fall well outside the single-photon resonant region. This is an indication that the pulse has also induced some transitions through multi-photon modes. Since the pulse duration is tuned in to given valence and conduction band states, some of the transitions may not be complete ($P_{CV} < 1$) and may take place outside the single and multi-photon resonance regions. Though more accentuated in the linear case (Fig. 7), both plots are consistently anisotropic. Under linearly polarized light the lack of rotational invariance is due to the preferred orientation of the polarization direction. In contrast, the origin of the anisotropy produced in the transition probability by circularly polarized light is two-fold: the un-matching velocities, i.e. $v_x \neq v_y$, and the field's initial phase δ.

VIII.   CONCLUSIONS

We have analyzed the quasienergy-spectrum and the valence to conduction band transition probability of an anisotropic tilted Dirac material subject to an arbitrarily intense electromagnetic field. The weak and strong field regimes have been studied as well as the linear and circular polariztions. The quasienergy-spectrum in the weak field regime strongly resembles the energy-spectrum of free carries regardless of the field polarization. At the crossover between the weak and the strong field regimes in $k = eE/\hbar\omega$, the structure of the quasi spectrum changes abruptly. Mainly two kinds of deviations with respect to free carriers can be identified in the strong field regime. The first type of deviation corresponds to deformation of the spectra in $\boldsymbol{k}$-space. Within the strong field region, where $k < eE/\hbar\omega$, the spectrum stretches as the electronic parameters renormalize due to electronic-dressing. Under linearly polarized light this deformation occurs exclusively in the direction perpendicular to the field polarization. On the contrary, circularly polarized light stretches the quasienergy spectrum in both, k_x and k_y directions. The second type of deviation is associated with the formation of gaps. Linearly polarized light produces a complicated pattern of new gaps and Dirac points around the original one located in $k_x = k_y = 0$. Instead, circularly polarized light opens up a gap in $k_x = k_y = 0$.

In the weak-field regime the light-matter coupling is perturbative and consequently the free carrier conic quasienergy spectrum remains almost unaltered. Hence, in this limit the electromagnetic field merely induces transitions between the quantum levels of free carriers without modifying their spectrum. Full transitions are therefore strictly constrained by the single photon resonance condition $2\epsilon(\boldsymbol{k}) = \omega$. For a linearly polarized pulse of a given duration not all of the transitions that comply with the resonant condition might take place due to the directional fluctuation of the transition time. Put another way, there are transitions that require very long

transition times and therefore do not fully occur. Circularly polarized pulses produce very symmetrical patterns with very smooth variations caused by the small fluctuations of the transition time and the anisotropic velocities.

Strong electromagnetic fields, on the other hand, profoundly distort the quasienergy spectrum. Thus, in the strong-field regime, transitions that escape the single-photon resonance condition may take place. Linearly polarized pulses generate a pattern in the transition probability as a function of the $\boldsymbol{k}$ components that is oriented in agreement with the polarization direction. Quasi-spectra with almost perfect cylindrical symmetry are obtained under the action of circularly polarized pulses. The small deviations from circular symmetry are due to the anisotropic velocities ($v_x \neq v_y$) and the initial phase δ of the radiation pulse.

To obtain many of the previous results, a new method to compute the time evolution operator in quantum mechanics was developed. This method, based on the determination of the monodromy matrix, has further capacities that were not exploited in this work. Among other things, in combination with the density matrix approach it can be used to compute non-linear electrical currents to examine light-field-driven currents in Dirac materials. Another application of this approach is the study of high harmonic generation.

* akb@azc.uam.mx
† jcarlosss@fisica.unam.mx
‡ vickkun@fisica.unam.mx
§ naumis@fisica.unam.mx

[1] F. Bonaccorso, Z. Sun, T. Hasan, and A. Ferrari, Nature photonics **4**, 611 (2010).

[2] Q. Bao, H. Hoh, and Y. Zhang, *Graphene Photonics, Optoelectronics, and Plasmonics* (CRC Press, 2017).

[3] J. S. Ponraj, Z.-Q. Xu, S. C. Dhanabalan, H. Mu, Y. Wang, J. Yuan, P. Li, S. Thakur, M. Ashrafi, K. Mccoubrey, *et al.*, Nanotechnology **27**, 462001 (2016).

[4] P. Saln, M. Basini, S. Bonetti, J. Hebling, M. Krasilnikov, A. Y. Nikitin, G. Shamuilov, Z. Tibai, V. Zhaunerchyk, and V. Goryashko, Physics Reports **836-837**, 1 (2019), matter manipulation with extreme terahertz light: Progress in the enabling THz technology.

[5] A. Grigorenko, M. Polini, and K. Novoselov, Nature photonics **6**, 749 (2012).

[6] Y. Fan, N.-H. Shen, F. Zhang, Q. Zhao, H. Wu, Q. Fu, Z. Wei, H. Li, and C. M. Soukoulis, Advanced Optical Materials **7**, 1800537 (2019).

[7] D. Wu, J. Guo, J. Du, C. Xia, L. Zeng, Y. Tian, Z. Shi, Y. Tian, X. J. Li, Y. H. Tsang, and J. Jie, ACS Nano **13**, 9907 (2019), pMID: 31361122, https://doi.org/10.1021/acsnano.9b03994.

[8] M. Scagliotti, M. Salvato, M. D. Crescenzi], N. Kovalchuk, I. Komissarov, S. Prischepa, D. Catone, L. D. Mario], M. Boscardin, M. Crivellari, and P. Castrucci, Carbon **152**, 643 (2019).

[9] M. Liu, X. Yin, E. Ulin-Avila, B. Geng, T. Zentgraf, L. Ju, F. Wang, and X. Zhang, Nature **474**, 64 (2011).

[10] V. Sorianello, M. Midrio, G. Contestabile, I. Asselberghs, J. Van Campenhout, C. Huyghebaert, I. Goykhman, A. Ott, A. Ferrari, and M. Romagnoli, Nature Photonics **12**, 40 (2018).

[11] R. Hao, J. Jiao, X. Peng, Z. Zhen, R. Dagarbek, Y. Zou, and E. Li, Optics letters **44**, 2586 (2019).

[12] A. Safaei, S. Chandra, M. W. Shabbir, M. N. Leuenberger, and D. Chanda, Nature communications **10**, 1 (2019).

[13] Z. Yin, J. Zhu, Q. He, X. Cao, C. Tan, H. Chen, Q. Yan, and H. Zhang, Advanced energy materials **4**, 1300574 (2014).

[14] P. Okeeffe, D. Catone, A. Paladini, F. Toschi, S. Turchini, L. Avaldi, F. Martelli, A. Agresti, S. Pescetelli, A. Del Rio Castillo, *et al.*, Nano letters **19**, 684 (2019).

[15] A. H. Castro Neto, F. Guinea, N. M. R. Peres, K. S. Novoselov, and A. K. Geim, Rev. Mod. Phys. **81**, 109 (2009).

[16] T. Higuchi, C. Heide, K. Ullmann, H. B. Weber, and P. Hommelhoff, Nature **550**, 224 (2017).

[17] C. Heide, T. Higuchi, H. B. Weber, and P. Hommelhoff, Phys. Rev. Lett. **121**, 207401 (2018).

[18] I. Orfanos, I. Makos, I. Liontos, E. Skantzakis, B. Frg, D. Charalambidis, and P. Tzallas, APL Photonics **4**, 080901 (2019), https://doi.org/10.1063/1.5086773.

[19] F. Krausz and M. I. Stockman, Nature Photonics **8**, 205 (2014).

[20] M. Hentschel, R. Kienberger, C. Spielmann, G. A. Reider, N. Milosevic, T. Brabec, P. Corkum, U. Heinzmann, M. Drescher, and F. Krausz, Nature **414**, 509 (2001).

[21] T. Oka and H. Aoki, Phys. Rev. B **79**, 081406 (2009).

[22] J. W. McIver, B. Schulte, F.-U. Stein, T. Matsuyama, G. Jotzu, G. Meier, and A. Cavalleri, Nature Physics **16**, 38 (2020).

[23] F. J. Lopez-Rodriguez and G. G. Naumis, Phys. Rev. B **78**, 201406(R) (2008).

[24] F. López-Rodríguez and G. Naumis, Philosophical Magazine **90**, 2977 (2010).

[25] O. V. Kibis, Phys. Rev. B **81**, 165433 (2010).

[26] H. L. Calvo, H. M. Pastawski, S. Roche, and L. E. F. F. Torres, Applied Physics Letters **98**, 232103 (2011), https://doi.org/10.1063/1.3597412.

[27] D. Sun, G. Aivazian, A. M. Jones, J. S. Ross, W. Yao, D. Cobden, and X. Xu, Nature nanotechnology **7**, 114 (2012).

[28] K. Kristinsson, O. V. Kibis, S. Morina, and I. A. Shelykh, Scientific Reports **6**, 20082 EP (2016).

[29] K. Kristinsson, O. V. Kibis, S. Morina, and I. A. Shelykh, Scientific reports **6**, 1 (2016).

[30] O. Kibis, K. Dini, I. Iorsh, and I. Shelykh, Physical Review B **95**, 125401 (2017).

[31] O. Kibis, K. Dini, I. Iorsh, V. Dragunov, and I. Shelykh, Journal of Structural Chemistry **59**, 867 (2018).

[32] H. L. Calvo, H. M. Pastawski, S. Roche, and L. E. F. F. Torres, Applied Physics Letters **98**, 232103 (2011), https://doi.org/10.1063/1.3597412.

[33] J. Sandoval-Santana, V. Ibarra-Sierra, A. Kunold, and G. G. Naumis, arXiv preprint arXiv:2003.12119 (2020).

[34] A. E. Champo and G. G. Naumis, Physical Review B **99**, 1 (2019).

[35] V. Ibarra-Sierra, J. Sandoval-Santana, A. Kunold, and G. G. Naumis, Physical Review B **100**, 125302 (2019).

[36] N. Goldman and J. Dalibard, Phys. Rev. X **4**, 031027 (2014).

[37] J. C. Sandoval-Santana, V. G. Ibarra-Sierra, J. L. Cardoso, A. Kunold, P. Roman-Taboada, and G. Naumis, Annalen der Physik **531**, 1900035 (2019), https://onlinelibrary.wiley.com/doi/pdf/10.1002/andp.201900035.

[38] T. Kitagawa, T. Oka, A. Brataas, L. Fu, and E. Demler, Phys. Rev. B **84**, 235108 (2011).

[39] B. Peng, H. Zhang, H. Shao, Y. Xu, R. Zhang, and H. Zhu, Journal of Materials Chemistry C **4**, 3592 (2016).

[40] S. Verma, A. Mawrie, and T. K. Ghosh, Physical Review B **96**, 155418 (2017).

[41] J. W. Villanova and K. Park, Phys. Rev. B **93**, 085122 (2016).

[42] A. D. Zabolotskiy and Y. E. Lozovik, Physical Review B **94**, 1 (2016).

[43] S. A. Herrera and G. G. Naumis, Phys. Rev. B **100**, 195420 (2019).

[44] J. J. Sakurai and E. D. Commins, "Modern quantum mechanics, revised edition," (1995).

[45] J. H. Shirley, Phys. Rev. **138**, B979 (1965).

[46] F. Verhulst, *Nonlinear Differential Equations and Dynamical Systems*, Universitext (Springer Berlin Heidelberg, 2006).

[47] J. K. Hale, "Ordinary differential equations. mineola, ny," (2009).

[48] M. A. Mojarro, V. G. Ibarra-Sierra, J. C. Sandoval-Santana, R. Carrillo-Bastos, and G. G. Naumis, Phys. Rev. B **101**, 165305 (2020).

[49] T. Dittrich, *Quantum transport and dissipation* (Wiley-VCH, 1998).

[50] D. Snoke, *Solid State Physics: Essential Concepts* (Cambridge University Press, 2020).

[51] D. Dubbers and H.-J. Stöckmann, *Quantum physics: the bottom-up approach: from the simple two-level system to irreducible representations* (Springer Science & Business Media, 2013).